

Realistic pattern formations on rough surfaces^{*}

Siqing LI[†] Leevan LING[‡] Steven J. RUUTH[§]

Xuemeng Wang[¶]

January 31, 2023

Abstract

We are interested in simulating patterns on rough surfaces. First, we consider periodic rough surfaces with analytic parametric equations, which are defined by some superposition of wave functions with random frequencies and angles of propagation. The amplitude of such surfaces is also an important variable in the provided eigenvalue analysis for the Laplace-Beltrami operator and in our numerical studies. Simulations show that the patterns become irregular as the amplitude and frequency of the rough surface increase. Next, for the sake of easy generalization to closed manifolds, we propose another construction method of rough surfaces by using random nodal values and discretized heat filters. We provide numerical evidence that both surface constructions yield comparable patterns to those found in real-life animals.

keywords Laplace-Beltrami operator, reaction-diffusion system, random surfaces, Turing pattern

AMS subject classifications 65M06, 35K57

1 Introduction

Pattern formation by reaction-diffusion systems has been an intensively studied field for decades. In 1952, Turing proposed the idea of diffusion-driven instability [47], in which simple mechanisms evolve from a homogeneous state into spatial heterogeneous patterns. In recent years, a variety of application areas have

^{*}This work was funded by the Hong Kong Research Grant Council GRF Grants (12303818, 12301419, 12301520), a National Youth Science Foundation of China (12201449), and the financial support of NSERC Canada (RGPIN-2022-03302).

[†]College of Data Science, Taiyuan University of Technology, Shanxi, China (lisiqing@tyut.edu.cn).

[‡]Department of Mathematics, Hong Kong Baptist University, Kowloon Tong, Hong Kong (lling@hkbu.edu.hk).

[§]Department of Mathematics, Simon Fraser University, Burnaby, British Columbia, Canada V5A1S6 (sruuth@sfu.ca).

[¶]Department of Mathematics, University of British Columbia, Vancouver, Canada, and Department of Mathematics, Hong Kong Baptist University, Kowloon Tong, Hong Kong (17251109@life.hkbu.edu.hk).

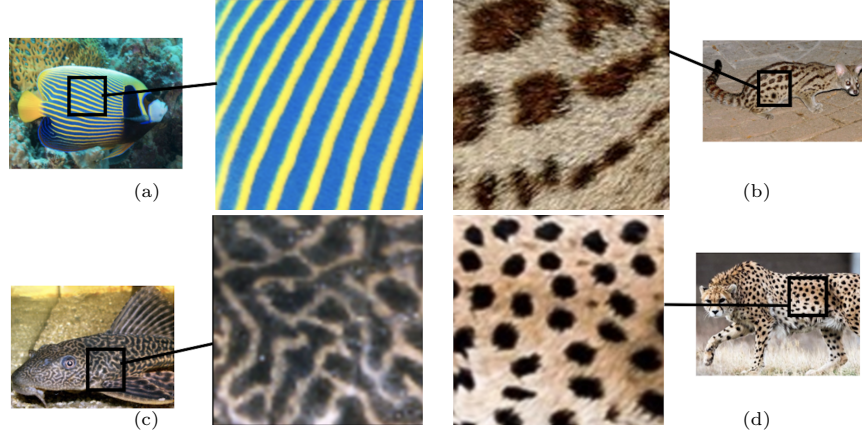


Figure 1: Skin patterns in real-life: (a) emperor angelfish [26], (b) genet [1], (c) pecestomus [12], (d) cheetah [46].

been actively developed, including vegetation pattern, plant root hair initiation, flock simulation and boundary drop configurations [4, 7, 13, 32]. Mechanisms of pattern generation under different types of transport or domain size have been considered as well; see [6, 25]. In theoretical biology, reaction-diffusion systems provide a relatively generic and concise approach for simulating animal skin patterns [18, 35], as well as regenerative processes of organisms [21]. In particular, reaction-diffusion systems are a well-accepted class of models for multiple pigmentation processes. Examples include marine [27] and emperor [26] angelfish, genets [1], plecostomi [12], cheetah [46], zebra fish [2], and many other mammal skin patterns [34]; see Figure 1. Although animal skin pattern simulation through reaction-diffusion systems has been explored in many researches, see the second row of Figure 5 for typical examples, very few of them have taken the skin texture into account. In reality, the skin surfaces are often rugged, and consequently the pattern will actually not be regular spots or stripes. Therefore, combining surface properties with reaction-diffusion systems can provide an opportunity for improved simulation of real pattern. In [11, 30], parameter functions instead of constants were used in PDEs to generate nonuniform and complex, i.e., more real-life, patterns.

Characterizing random rough surfaces can be carried out by a variety of methods. These include the reference parameter method, motif method, fractal method, watershed method, and wavelet method, etc [42]. For three-dimensional surface topography, there are a number of parameters involved [20]. To generate random rough surfaces, both the Fast Fourier Transform (FFT) [37] and digital filter [23] methods can be applied to approximate the auto-correlation function for surfaces with wavelengths. In [24], the authors proposed an approach that applies the covariance function and Karhunen-Loève expansion to generate random surfaces. Rough surfaces may also be generated from spatial frequencies via the FFT method; in this case, the rough surface is built by summing up

trigonometric functions [43].

In Section 2, the rough surface \mathcal{M} with parametric equations will be formulated in detail. We consider periodic rough surfaces \mathcal{M} characterized with spatial frequency, which come with analytic parametric equations. In Section 5, we consider surfaces \mathcal{S} constructed by random nodal values and discretized heat filters. The latter surface construction technique can be easily extended to add “roughness” to more general manifolds. Along with the construction of rough surfaces, we will review the concept of the heat equation which is a surface PDE involving the Laplace operator on manifolds.

Moving from a flat geometry to rough surfaces, generally speaking, we have to deal with surface dependent differential operators. Surface PDEs have been extensively studied in recent years, and there are a variety of techniques for their analysis and computation. The approaches for surface PDEs can be separated into intrinsic methods and embedding methods. Intrinsic methods solve PDEs on the manifold directly. However, embedding methods formulate and solve PDEs on a band around the manifold. Intrinsic and embedding methods that are dependent on mesh construction have been explored by many researchers. Examples of such methods include finite difference [40], finite element [5, 16, 36], and finite volume [14, 15] methods. There are also numerical methods that do not require meshes, namely meshfree methods. Meshfree methods for surface PDEs, such as radial basis function (RBF) methods [8–10, 19] and the meshfree generalized finite difference method [44, 45], have the advantage of avoiding mesh construction.

In Section 3, we apply the finite difference method to solve pattern formation PDEs on rough surfaces \mathcal{M} ; the FDM is chosen because of its simplicity and effectiveness on the class of problem domains considered. The rough surface pattern formation models here are not yet extendable to add roughness to other manifolds, e.g., we cannot yet create red-blood cells with rough surfaces. Our aim is to study the effect of roughness on pattern formation using the simplest setup. Numerical simulation results on rough surfaces \mathcal{M} with parametric equations are demonstrated in Section 4.

In Section 5, we put forward a different construction method of rough surfaces \mathcal{S} by random discrete data. After updating our numerical schemes for \mathcal{M} to work on \mathcal{S} , we see that surface types \mathcal{M} and \mathcal{S} yield comparable patterns. In Section 4 and Section 5, we present some simulated animal coat patterns on both types of surfaces, \mathcal{M} and \mathcal{S} . Results for PDEs with constant parameters on rough surfaces with various roughness are similar to the real-life patterns displayed in Figure 1.

2 Rough surfaces \mathcal{M} with analytic parametric equations

Consider \mathcal{C}^k -smooth ($k \geq 2$), codimension 1, and periodic Riemannian surfaces

$$\mathcal{M} = \{(x, y, z) \in \mathbb{R}^3 : z = z(x, y) \text{ for } (x, y) \in V \subset \mathbb{R}^2\}, \quad (1)$$

for some \mathcal{C}^k function $z(\cdot, \cdot)$ defined on a global parameter space $V \subset \mathbb{R}^2$. A corresponding parametric representation of \mathcal{M} is given by

$$\vec{r}(x, y) = [x, y, z(x, y)]^T \in \mathcal{M}, \quad (x, y) \in V.$$

For convenience, let $(x, y) := (x_1, x_2)$; we shall use both notations interchangeably. Recall that the first fundamental form $G : V \rightarrow \mathbb{R}^{2 \times 2}$ of \mathcal{M} is defined by

$$G(x, y) = \begin{bmatrix} g_{11} & g_{12} \\ g_{21} & g_{22} \end{bmatrix} (x, y) \quad \text{where} \quad g_{ij}(x, y) = \frac{\partial \vec{r}(x, y)}{\partial x_i} \cdot \frac{\partial \vec{r}(x, y)}{\partial x_j},$$

see [16] for a review. In the case of a surface function \mathcal{M} as in (1), we have

$$G(x, y) = \begin{bmatrix} g_{11} & g_{12} \\ g_{21} & g_{22} \end{bmatrix} (x, y) = \begin{bmatrix} 1 + z_x^2 & z_x z_y \\ z_x z_y & 1 + z_y^2 \end{bmatrix}, \quad (2)$$

whose determinant and inverse are

$$g(x, y) := \det(G)(x, y) = 1 + z_x^2 + z_y^2, \quad (3)$$

and

$$G^{-1}(x, y) = \begin{bmatrix} g^{11} & g^{12} \\ g^{21} & g^{22} \end{bmatrix} (x, y) = \frac{1}{1 + z_x^2 + z_y^2} \begin{pmatrix} 1 + z_y^2 & -z_x z_y \\ -z_x z_y & 1 + z_x^2 \end{pmatrix}. \quad (4)$$

Using (3)–(4), the Laplace-Beltrami operator on \mathcal{M} is given by

$$\Delta_{\mathcal{M}} f = \frac{1}{\sqrt{g}} \sum_{1 \leq i, j \leq 2} \frac{\partial}{\partial x_i} \left(\sqrt{g} g^{ij} \frac{\partial}{\partial x_j} f \right) =: \frac{1}{\sqrt{g}} \nabla \cdot (\mathcal{A} \nabla f), \quad (5)$$

for any \mathcal{C}^2 function $f : \mathcal{M} \rightarrow \mathbb{R}$.

Now, we focus on random rough surfaces $\mathcal{M} \subseteq \mathbb{R}^3$ in the form of (1), whose surface function $z : \mathcal{I}^2 = [-L, L]^2 \rightarrow \mathbb{R}$ is a superposition of elementary waves [17, 43]. The function z is stochastically determined by

$$z(x, y) = \sum_{m=-M}^M \sum_{n=-N}^N a_{m,n} \cos \left(2\pi(mx + ny) + \phi_{m,n} \right), \quad (6)$$

for some random variables $a_{m,n}$ and $\phi_{m,n}$. Similar to a Fourier series expansion, $z(x, y)$ in (6) is constructed by trigonometric functions in which m, n correspond to spatial frequencies on the x and y axes respectively. As in [43], the spatial frequencies m and n allow values taken up to maximum integers M and N respectively; this corresponds to a high frequency cut off.

To determine (6), we first introduce $\tilde{a}_{m,n} \sim \mathcal{N}(0, 1)$ and $\phi_{m,n} \sim \mathcal{U}(0, \pi)$. This specifies the pre-surface function $\tilde{z} = \tilde{z}(x, y)$. Next, we control the amplitude of the rough surface \mathcal{M} to be within a specific range $[-\delta_{\mathcal{M}}, \delta_{\mathcal{M}}]$ by scaling according to

$$z := \frac{\delta_{\mathcal{M}}}{\|\tilde{z}\|_{\infty}} \tilde{z}, \quad \text{i.e., } a_{m,n} := \frac{\delta_{\mathcal{M}}}{\|\tilde{z}\|_{\infty}} \tilde{a}_{m,n}. \quad (7)$$

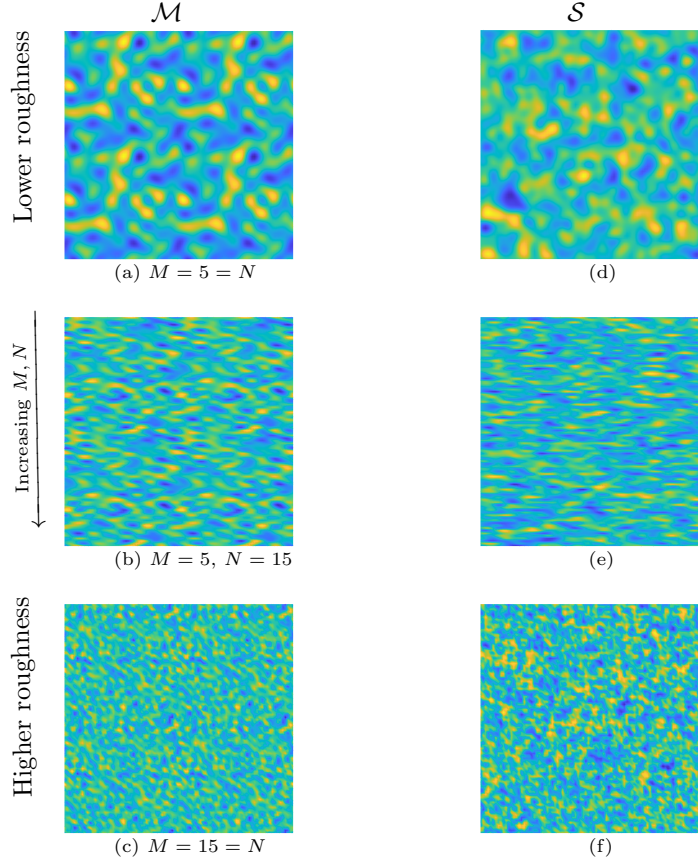


Figure 2: Bird's-eye view of some random rough surfaces \mathcal{M} from Section 2 (left) and \mathcal{S} from Section 5 (right).

Figures 2 (a)–(c), first column, show some rough surfaces \mathcal{M} with amplitude $\delta_{\mathcal{M}} = 10^{-3}$ and various (M, N) . The construction of the rough surfaces \mathcal{S} appearing in the second column will be discussed in Section 5.

Remark: One can also add a decay condition with respect to frequencies m, n and a frequency attenuation parameter β to the pre-coefficient $\tilde{a}_{m,n}$ via

$$\tilde{a}_{m,n} \sim \frac{1}{(m^2 + n^2)^{\beta/2}} \mathcal{N}(\mu, \sigma).$$

2.1 Surface roughness and Laplace-Beltrami operator

Applying the definition of the Laplace-Beltrami operator (5) to the rough surface function in (6)–(7), the relationship between the eigenvalues of the diffusion tensor and the geometry of the surface can be made explicit. Firstly, the *diffu-*

sion tensor \mathcal{A} in (5) is

$$\mathcal{A}(x, y) = \begin{bmatrix} \mathcal{A}_1 & \mathcal{A}_2 \\ \mathcal{A}_2 & \mathcal{A}_4 \end{bmatrix} (x, y) := \sqrt{g} G^{-1} = \frac{1}{\sqrt{g}} \begin{bmatrix} 1 + z_y^2 & -z_x z_y \\ -z_x z_y & 1 + z_x^2 \end{bmatrix}, \quad (8)$$

with the partial derivatives z_x and z_y computing from (6). We are interested in obtaining the eigenvalues and eigenvectors of \mathcal{A} . Rather than computing these quantities directly, it turns out to be easier to first compute the eigenvalues and eigenvectors of the Riemannian metric tensor G in (2). From the characteristic equation of G

$$|G - \lambda I| = (1 + z_x^2 - \lambda)(1 + z_y^2 - \lambda) - z_x^2 z_y^2 = 0,$$

we find that the eigenvalues λ^G of G are $1 + z_x^2 + z_y^2 = g$ and 1. Since

$$\mathcal{A}\vec{v} = \sqrt{g} G^{-1} \vec{v} = \frac{\sqrt{g}}{\lambda^G} \vec{v}, \quad (9)$$

any eigenvector \vec{v} of G is also an eigenvector of \mathcal{A} and the eigenvalues $\lambda^{\mathcal{A}}$ of \mathcal{A} are

$$\lambda^{\mathcal{A}} = \left\{ \sqrt{g} = \sqrt{1 + z_x^2 + z_y^2}, \frac{1}{\sqrt{g}} \right\}. \quad (10)$$

Note that, by (7), the matrix function $[G - \lambda^G I](z_x, z_y) = C(\delta_{\mathcal{M}})[G - \lambda^G I](\tilde{z}_x, \tilde{z}_y)$ for some $\delta_{\mathcal{M}}$ -dependent constant $C(\delta_{\mathcal{M}})$. This implies that all eigendirections of G (and \mathcal{A}) are independent of the amplitude $\delta_{\mathcal{M}}$. Simple calculations show that $\lambda^{\mathcal{A}} = 1 + \mathcal{O}(M^2 N^2 \delta_{\mathcal{M}}^2)$ varies with $\delta_{\mathcal{M}}$ nonlinearly by a bijection. Thus, the contour lines (but not the height) of $\lambda^{\mathcal{A}}$ are independent of $\delta_{\mathcal{M}}$.

Figure 3 illustrates the close relationship between the eigenvalues of \mathcal{A} and the geometric properties of a rough surface. In particular, we can see from subfigures (b), (c), and (e) that the maximum (and minimum) eigenvalues are larger (and smaller) at regions of the surface with the steepest gradients. In subfigures (d) and (f), eigendirections are plotted on top of subfigure (b). We can clearly see that the eigenvectors corresponding to the maximum (and minimum) eigenvalues are tangent (and orthogonal) to the contour plots of eigenvalues.

3 Solving heat equations on rough surfaces \mathcal{M}

We begin by constructing a finite difference scheme for solving heat equations on rough surfaces $\mathcal{M} \subset \mathbb{R}^3$ defined by (6)–(7). We work intrinsically by transforming the PDEs on rough surfaces to the parameter space $\mathcal{I}^2 = [-L, L]^2 \subset \mathbb{R}^2$. Subsequently, we move on to solving reaction-diffusion systems for pattern formation.

We consider the heat equation on a rough surface

$$\frac{\partial u}{\partial t}(\xi, t) - \Delta_{\mathcal{M}} u(\xi, t) = h(\xi, t) \quad \text{for } \xi \in \mathcal{M}, t \in (0, T], \quad (11a)$$

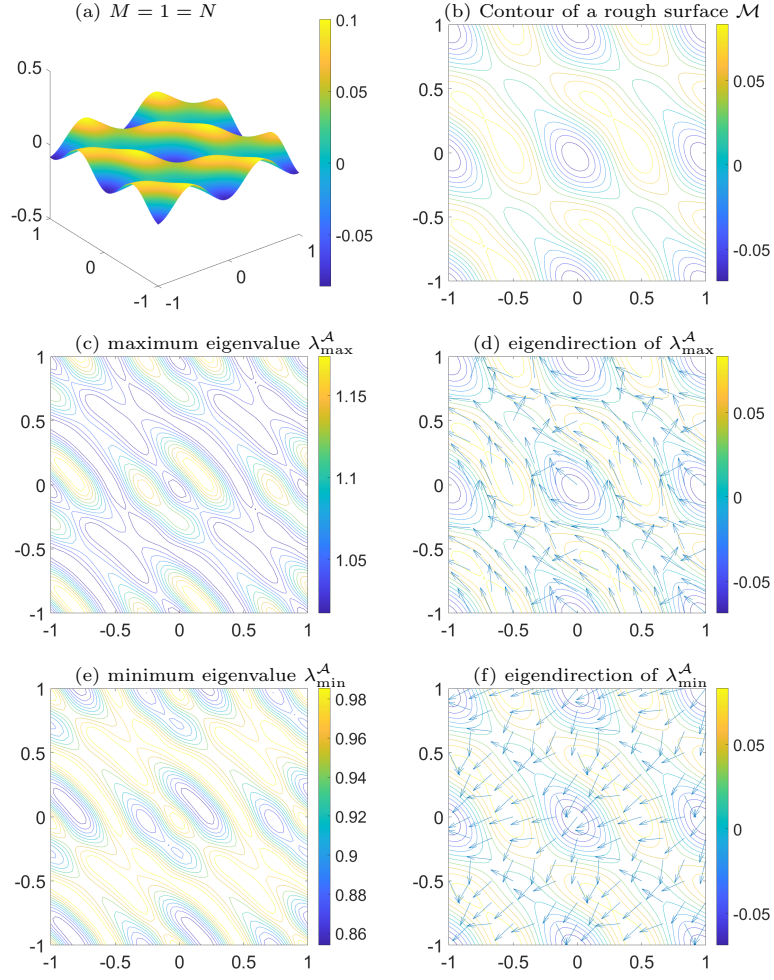


Figure 3: (a, b): 3D and contour plots of a rough surface in the form of (7) with $M = N = 1$ and amplitude $\delta_{\mathcal{M}} = 1E - 1$, (c, d): maximum eigenvalue and eigendirection of \mathcal{A} , (e, f): minimum eigenvalue and eigendirection of \mathcal{A} .

where $u : \mathcal{M} \times (0, T] \rightarrow \mathbb{R}$, subject to periodic boundary conditions on $\partial\mathcal{M} := \partial\mathcal{I}^2 \times z(\partial\mathcal{I}^2)$ with $z(\partial\mathcal{I}^2)$ being the surface function in (6), i.e.,

$$\begin{aligned} u([-L, y, z(-L, y)]^T, t) &= u([L, y, z(L, y)]^T, t), \quad \text{for } y \in \mathcal{I}, \quad t \in (0, T], \\ u([x, -L, z(x, -L)]^T, t) &= u([x, L, z(x, L)]^T, t), \quad \text{for } x \in \mathcal{I}, \quad t \in (0, T]. \end{aligned} \quad (11b)$$

Since all surface points are in the form $\xi = [x, y, z(x, y)]^T \in \mathcal{M}$ for $[x, y]^T \in \mathcal{I}^2$ and z in (6), we discretize the parameter space \mathcal{I}^2 by some set of $n_X n_Y$ tensor-product grid points $[X, Y] \in \mathbb{R}^{n_X n_Y \times 2} \subset \mathcal{I}^2$. Let $u^j(x, y) \approx u([x, y, z(x, y)]^T, t^j)$ for $[x, y]^T \in \mathcal{I}^2$. We begin by temporal discretization of (11a) by the θ -method

$$\frac{u^{j+1} - u^j}{\tau} = \theta(\Delta_{\mathcal{M}} u^{j+1} + h^{j+1}) + (1 - \theta)(\Delta_{\mathcal{M}} u^j + h^j), \quad (12)$$

for an equispaced partition $\{t^j\}_{j=0}^M$ of $[0, T]$ with step-size τ . By some user-selected finite difference scheme for the first derivative, we construct differentiation matrices $\mathcal{D}_k \in \mathbb{R}^{n_X n_Y \times n_X n_Y}$ such that, for any C^1 -function $w : \mathcal{I}^2 \rightarrow \mathbb{R}$ satisfying periodic boundary condition (11b), we have

$$\mathcal{D}_k w(X, Y) \approx \frac{\partial w}{\partial x_k}(X, Y), \quad \text{for } k \in \{1, 2\},$$

where the $n_X n_Y \times 1$ vector $w(X, Y)$ (and $\frac{\partial w}{\partial x_k}(X, Y)$) contains nodal values of w (and $\frac{\partial w}{\partial x_k}$) at grid points in $[X, Y]$. Working directly on definitions (5)–(8), we can approximate the Laplace-Beltrami term $\Delta_{\mathcal{M}} w$ at grids $[X, Y]$ by nodal function values $W := w(X, Y)$ according to

$$\begin{aligned} \Delta_{\mathcal{M}} w(X, Y) &\approx \frac{1}{\sqrt{g}}(X, Y) \otimes \left(\mathcal{D}_1 \left(\mathcal{A}_1(X, Y) \otimes (\mathcal{D}_1 W) \right) + \mathcal{D}_2 \left(\mathcal{A}_4(X, Y) \otimes (\mathcal{D}_2 W) \right) \right. \\ &\quad \left. + \mathcal{D}_1 \left(\mathcal{A}_2(X, Y) \otimes (\mathcal{D}_2 W) \right) + \mathcal{D}_2 \left(\mathcal{A}_2(X, Y) \otimes (\mathcal{D}_1 W) \right) \right) \\ &= \frac{1}{\sqrt{g}}(X, Y) \odot \left[\mathcal{D}_1 \left(\mathcal{A}_1(X, Y) \odot \mathcal{D}_1 \right) + \mathcal{D}_2 \left(\mathcal{A}_4(X, Y) \odot \mathcal{D}_2 \right) \right. \\ &\quad \left. + \mathcal{D}_1 \left(\mathcal{A}_2(X, Y) \odot \mathcal{D}_2 \right) + \mathcal{D}_2 \left(\mathcal{A}_2(X, Y) \odot \mathcal{D}_1 \right) \right] W \\ &=: \Delta_{\mathcal{M}, h} W, \end{aligned} \quad (13)$$

where $\Delta_{\mathcal{M}, h} \in \mathbb{R}^{n_X n_Y \times n_X n_Y}$, \otimes is the element-wise Hadamard product of matrices and \odot is a vector-matrix product defined by $\vec{a} \odot [\vec{b}_1, \dots, \vec{b}_n] := [\vec{a} \otimes \vec{b}_1, \dots, \vec{a} \otimes \vec{b}_n]$. See Appendix for the detailed construction of differentiation matrices $\mathcal{D}_1, \mathcal{D}_2$. Combining (12) and (13) yields a fully discretized scheme for the update in time.

3.1 Visualizing heat flow on a rough surface \mathcal{M}

We show the heat flow under different amplitudes of rough surface \mathcal{M} in (3) by solving the heat equations (11a) with zero flux $h(\xi, t) = 0$ and periodic boundary

conditions (11b). The rough surfaces \mathcal{M} are defined over the parameter space $\mathcal{I}^2 = [-1, 1]^2 \subset \mathbb{R}^2$. The compatible initial condition is given by

$$u(x, y, z, 0) = \cos(\pi x/2) \cos(\pi y/2). \quad (14)$$

Figure 4 shows the numerical solutions on the surface \mathcal{M} in Figure 3 (b) with $\delta_{\mathcal{M}} \in \{0.1, 0.5, 1\}$ in the respective rows. In all cases, we use backward Euler method, and set $\tau = 1E - 3$, $T = 1$ and $n_X = 41 = n_Y$. Figure 4 shows that the range of the numerical solutions becomes larger as the amplitude of \mathcal{M} increases from $\delta_{\mathcal{M}} = 0.1$ to $\delta_{\mathcal{M}} = 1$. From the rough surface in Figure 3 (b) and solutions in Figure 4, it can be concluded that the heat flow when projected to the plane is greatest in flat regions.

4 Pattern formation on a rough surface \mathcal{M}

In this section, we consider reaction-diffusion systems (RDS) on a rough surface \mathcal{M}

$$\begin{cases} \partial_t u = \delta_u \Delta_{\mathcal{M}} u + f_u(u, v), \\ \partial_t v = \delta_v \Delta_{\mathcal{M}} v + f_v(u, v), \end{cases} \quad (15)$$

for some (concentration) functions $u, v : \mathcal{M} \times (0, T] \rightarrow \mathbb{R}$, and reaction terms

$$\begin{cases} f_u(u, v) = \alpha u(1 - \xi_1 v^2) + v(1 - \xi_2 u), \\ f_v(u, v) = \beta v \left(1 + \frac{\alpha \xi_1}{\beta} uv\right) + u(\gamma + \xi_2 v), \end{cases} \quad (16)$$

with parameters $\delta_u, \delta_v, \alpha, \beta, \xi_1, \xi_2$. Pattern formation on very smooth (and usually closed) surfaces with little variation is discussed in [10, 29, 33, 41]; pattern formation on rough surfaces has not been studied as far as the authors know. In this section, we aim to analyze the effect of rough surfaces on pattern formation generated by the reaction-diffusion system (15)-(16). Numerical methods are not our focus and we simply extend the finite difference scheme in the previous section to work here. Other options for the discretization of reaction-diffusion systems include the finite element method [22, 28, 38], and various types of mesh-free methods [30, 31].

As in Section 3, we work on an equispaced temporal partition $\{t^j\}_{j=0}^{N_T}$ with some time step-size $\tau > 0$ and tensor-product grid points $[X, Y] \in \mathbb{R}^{n_X n_Y \times 2} \subset \mathcal{I}^2$. Let

$$U^j \approx u(X, Y, z(X, Y), t^j) \quad \text{and} \quad V^j \approx v(X, Y, z(X, Y), t^j), \quad 1 \leq j \leq N_T,$$

be the unknown nodal values we seek based on initial conditions U^0 and V^0 . Using the second order backward differentiation formula (BDF2) [3, 39] and (13) to discretize the RDS (15) with periodic boundary condition (11b), we obtain

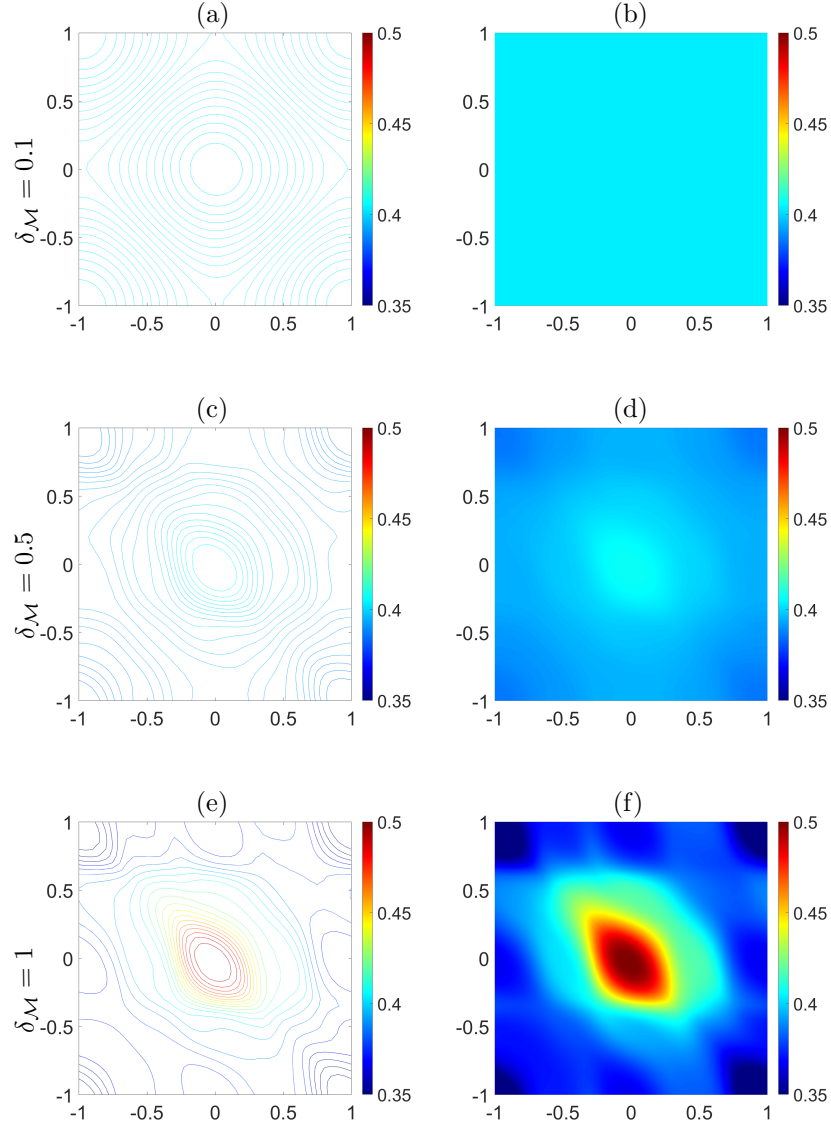


Figure 4: Numerical solution of heat equations under different amplitudes $\delta_{\mathcal{M}}$. (a, b): $\delta_{\mathcal{M}} = 0.1$, (c, d): $\delta_{\mathcal{M}} = 0.5$, (e, f): $\delta_{\mathcal{M}} = 1$. In all cases, $\tau = 1E - 3$, $T = 1$, $n_X = 41 = n_Y$.

Table 1: Parameters of the reaction-diffusion system (15)-(16) for generating spots and stripes patterns on rough surfaces.

Pattern	δ_v	δ_u	α	β	γ	ξ_1	ξ_2
Spots	10^{-3}	$0.516\delta_v$	0.899	-0.91	-0.899	0.02	0.2
Stripes	10^{-3}	$0.516\delta_v$	0.899	-0.91	-0.899	3.5	0

the following fully-discrete system of equations on \mathcal{M}

$$\begin{cases} 3U^{j+1} - 2\tau\delta_u\triangle_{\mathcal{M},h}U^{j+1} = 4\tau f_u(U^j, V^j) - 2\tau f_u(U^{j-1}, V^{j-1}) + 4U^j - U^{j-1}, \\ 3V^{j+1} - 2\tau\delta_v\triangle_{\mathcal{M},h}V^{j+1} = 4\tau f_v(U^j, V^j) - 2\tau f_v(U^{j-1}, V^{j-1}) + 4V^j - V^{j-1}, \end{cases} \quad (17)$$

for $1 \leq j \leq N_T$, subject to some yet-to-be specified (usually random) initial condition and some first order approximations to the solutions at the first time step, U^1 and V^1 . Note that the two equations in (17) are not coupled; the computational cost is of the same order as that of solving two scalar heat equations.

4.1 The pattern generation process

In this subsection, we show the formation of irregular patterns as we go from a flat two dimensional domain to rough surfaces with different amplitudes. We start with patterns on the flat domain $[-1, 1]^2$ as in [30], i.e., the rough surface with zero amplitude ($\delta_{\mathcal{M}} = 0$). Model and surface parameters are chosen according to the values in Table 1. To discretize, we select grid parameters $n_X = 90$, $n_Y = n_X$, and a time step-size $\tau = 0.5$. The rough surfaces \mathcal{M} with $M = N = 5$ are used in this part.

The first row of Figure 5 plots the initial conditions used to compute the spots and stripes patterns, respectively. These are random values generated within the interval $[-0.5, 0.5]$. The second row of Figure 5 shows the steady state patterns on the surface with zero amplitude. Perfect spots and stripes are obtained, which is similar to our previous results in [30]. Next, we set the initial conditions for the next amplitude to be the steady solutions from the zero amplitude rough surface, i.e, we use the solution of spots with $\delta_{\mathcal{M}} = 0$, $T = 800$ and the solution of stripes with $\delta_{\mathcal{M}} = 0$, $T = 4000$. By increasing the amplitude of the rough surface from $\delta_{\mathcal{M}} = 0$ to $\delta_{\mathcal{M}} = 0.1$ with increments of 0.01, and setting initial conditions using the previous steady state, we achieve the final patterns for $\delta_{\mathcal{M}} = 0.1$. These are shown in the third row of Figure 5. For rough surfaces under small amplitude $\delta_{\mathcal{M}} = 0.05$, the spots and stripes are similar to those with $\delta_{\mathcal{M}} = 0$. However, for larger amplitude $\delta_{\mathcal{M}} = 0.1$, both spots and stripes become irregular. We can conclude that the steady state patterns become irregular as the amplitude of the rough surface \mathcal{M} increases.

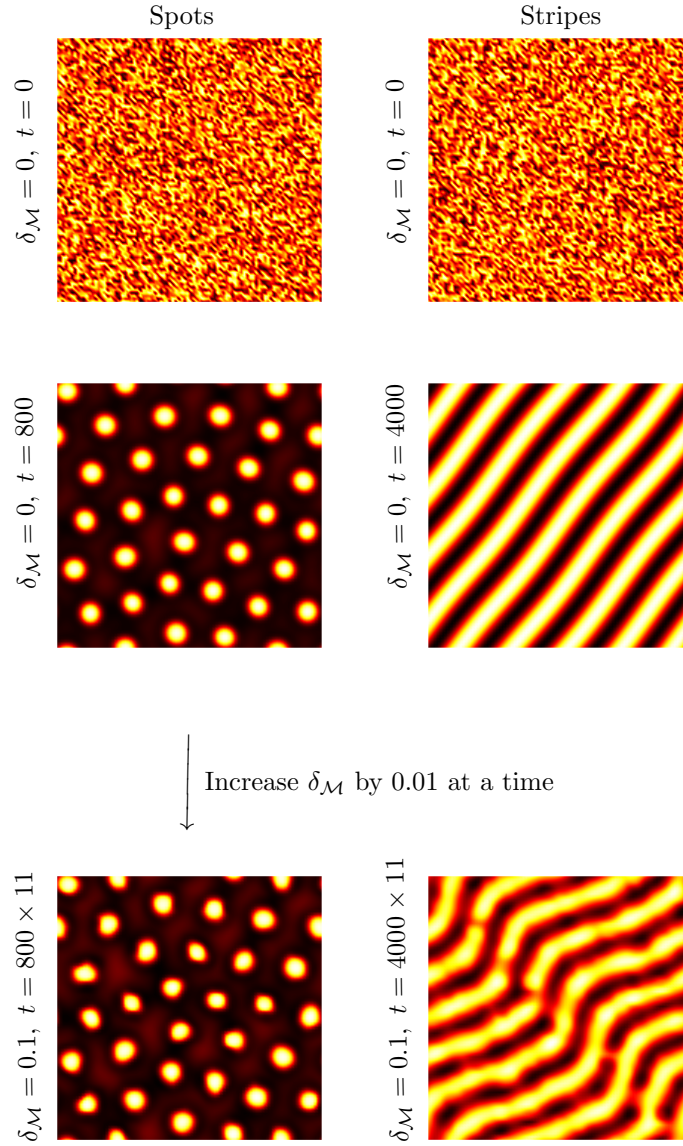


Figure 5: Pattern generation on rough surfaces \mathcal{M} with $M = N = 5$ and amplitude $\delta_{\mathcal{M}}$ increasing from 0 to 0.1. Parameters for spots and stripes are set according to Table 1. Discretization parameters are $n_X = 90 = n_Y$, $\tau = 0.5$.

4.2 Patterns on surfaces with different spatial frequencies and amplitudes

Properties of rough surfaces are influenced by the amplitude $\delta_{\mathcal{M}}$ and the spatial frequencies M, N in (7). To better understand patterns on rough surfaces with different properties, we compute steady state patterns for

$$\delta_{\mathcal{M}} \in \{0.05, 0.1\}, \quad (M, N) \in \{(5, 15), (15, 15)\},$$

on the parameter space $\mathcal{I}^2 = [-0.5, 0.5]^2 \subset \mathbb{R}^2$. Periodic boundary conditions on $\partial\mathcal{M} := \partial\mathcal{I}^2 \times z(\partial\mathcal{I}^2)$ are prescribed.

These patterns in both 2-D view and zoom in 3-D view are presented in Figures 6-7 for spots, and in Figures 8-9 for stripes. As before, the initial conditions are assigned to be random data in $[-0.5, 0.5]$. In order to capture details of the spot and stripe patterns, we increase the spatial resolution from $n_X = 90$ to $n_X = 170$, again keeping $n_Y = n_X$ to ensure the irregular patterns were due to the roughness rather than low resolution.

Firstly, from Figures 6 and 7, we can see that the number of spots increases as the frequencies M, N and the amplitude $\delta_{\mathcal{M}}$ increase. For fixed amplitude $\delta_{\mathcal{M}}$, patterns are deformed along the x -axis as the frequency N increases. This conclusion is clearly illustrated in the case $\delta_{\mathcal{M}} = 0.1$. On the other hand, for fixed values of M, N , the patterns maintain their shape as spots when $\delta_{\mathcal{M}} \leq 0.05$, and start to deform when $\delta_{\mathcal{M}} \geq 0.05$. For $\delta = 0.1$, all patterns become deformed spots.

Secondly, for fixed $\delta_{\mathcal{M}} = 0.05$, zoom in 3-D profiles of region $[-0.3, 0.1] \times [-0.3, 0]$ for $[M, N] = [5, 15]$ and region $[0.2, 0.5] \times [-0.3, 0]$ for $[M, N] = [15, 15]$ reveal that irregular spots appear when part of the pattern is located in a valley or ridge of the rough surface. When $\delta_{\mathcal{M}}$ increases to 0.1, as in Figure 7, the deformation of the patterns is more severe. This makes sense since the amplitude $\delta_{\mathcal{M}}$ is twice that of Figure 6. From zoom in 3-D figures of region $[-0.1, 0.5] \times [0.1, 0.4]$ for $[M, N] = [5, 15]$ and region $[-0.4, 0.1] \times [-0.2, 0.1]$ for $[M, N] = [15, 15]$, the deformed patterns again appear when their locations cover the local ridge/valley/mountain of the rough surfaces.

As frequencies and amplitudes are varied, similar behavior (to the case of spots) can be observed in stripe formation; see Figures 8 and 9. High amplitudes and frequencies yield a particularly strong effect in the zoom in 3-D plots in Figure 9, where the stripes break into small separate components. Further, we observe that the largest concentration values appear at the local peaks of the rough surface \mathcal{M} .

4.3 Animal coat simulation results

In simulation results on rough surfaces \mathcal{M} which are characterized by spatial frequencies, we observe interesting similarities between some steady state patterns and actual animal coat patterns. In Figure 10, we show the simulations of the animal coats in Figure 1 by patterns on rough surfaces \mathcal{M} . The specific

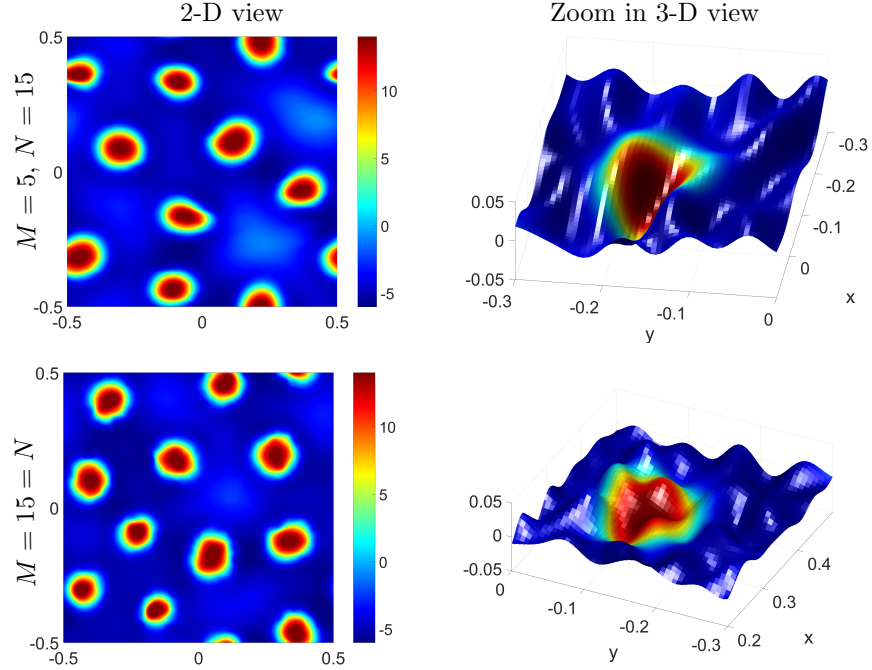


Figure 6: Patterns on rough surfaces with amplitude $\delta_{\mathcal{M}} = 0.05$. Discretization parameters are $n_X = 170 = n_Y$, $\tau = 0.5$, $T = 800$, $\mathcal{I}^2 := [-0.5, 0.5]^2$.

parameter values for generating each animal coat pattern are listed in Tables 1 and 2.

Table 2: Parameters for animal coats simulation on \mathcal{M} in Figure 10 with $n_X = n_Y = 90$

		M	N	τ	T	$\delta_{\mathcal{M}}$
Emperor angelfish [26]	Figure 10 (a)	5	5	0.5	4000	0.05
Genet [1]	Figure 10 (b)	15	15	0.5	800	0.1
Plecostomus [12]	Figure 10 (c)	15	5	0.5	4000	0.1
Cheetah [46]	Figure 10 (d)	15	5	0.5	800	0.1

5 Random rough surfaces \mathcal{S} by discrete data

While the parametric equation (6) allows us to work analytically on rough surfaces, i.e., via the evaluation of metric tensor (2), its generalization to manifolds [9, 10, 40] is not trivial.

In [24], the authors used the covariance function of random deformation fields and the surface Karhunen-Loève expansion to generate random surfaces. In [23], the authors applied the 2D digital filter and Fourier analysis to generate random rough surfaces. In this section, we introduce a new approach for constructing

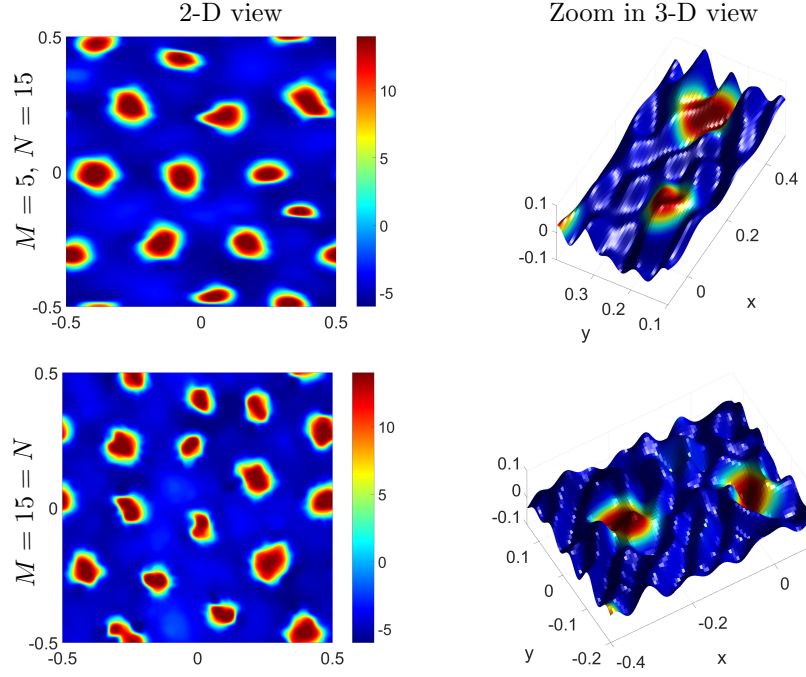


Figure 7: Patterns on rough surfaces with amplitude $\delta_{\mathcal{M}} = 0.1$. Discretization parameters are $n_X = 170 = n_Y, \tau = 0.5, T = 800, \mathcal{I}^2 := [-0.5, 0.5]^2$.

rough surfaces \mathcal{S} based on random data and heat filters. The desired reaction-diffusion systems are then solved on \mathcal{S} .

5.1 Construction of \mathcal{S} by heat filters

We want to generate some random rough surfaces \mathcal{S} , which have similar roughness as rough surfaces \mathcal{M} in (7) with different M and N .

Let $[X, Y] \in \mathbb{R}^{n_X n_Y \times 2} \subset \mathcal{I}^2$ as in Section 3. We assign uniform random numbers to each node to obtain the initial random surface values $\tilde{Z}_0 \sim (\mathcal{U}[-1, 1])^{n_X n_Y}$ at nodes $[X, Y]$. We define the discretized heat filter according to the method of Section 3 but with some filter-diffusion tensor \mathcal{F} (instead of the diffusion tensor \mathcal{A} for surface \mathcal{M}) in the Laplace-Beltrami operator $\Delta_{\mathcal{F}, h}$. For an isotropic filter, we take $\mathcal{F} = I_{2 \times 2}$. This can generate an \mathcal{M} -like surface with $M = N$. For the anisotropic case with $M \neq N$, we use $\mathcal{F} = \text{diag}(2, 1)$. We can now *smooth* the surface data J -times via

$$\tilde{Z}_{j+1} = (Q + \kappa h \Delta_{\mathcal{F}, h}) \tilde{Z}_j, \quad \text{for } j = 0, \dots, J,$$

where Q is an $n_X n_Y$ by $n_X n_Y$ matrix of ones, $\kappa > 0$ is the parameter to control the weights of $\Delta_{\mathcal{F}, h}$, and h is the fill distance of the discrete set. This completes the definition of the pre-surface that is the counterpart to \tilde{Z} in (7) of the surface

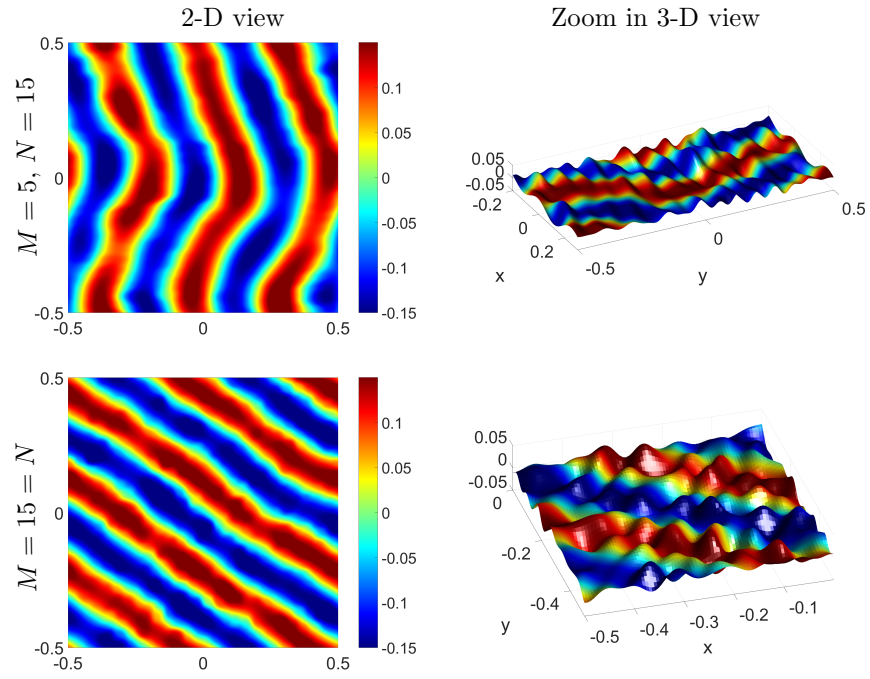


Figure 8: Patterns on rough surfaces with amplitude $\delta_{\mathcal{M}} \in \{0.05\}$ and $(M, N) \in \{(5, 15), (15, 15)\}$. The model parameters for stripes are set according to Table 1. Discretization parameters are $n_X = 170 = n_Y, \tau = 0.5, T = 4000$.

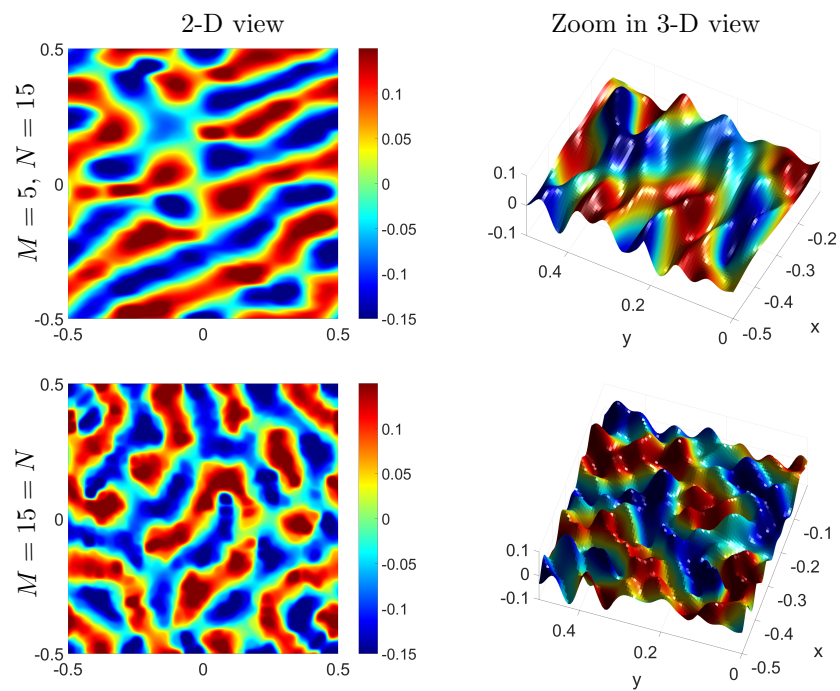
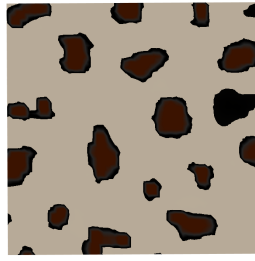


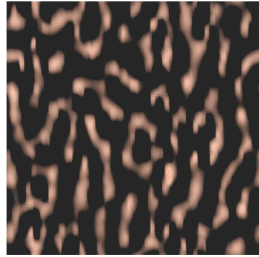
Figure 9: Patterns on rough surfaces with amplitude $\delta_{\mathcal{M}} = 0.1$ and $(M, N) \in \{(5, 15), (15, 15)\}$. The model parameters for stripes are set according to Table 1. Discretization parameters are $n_X = 170 = n_Y, \tau = 0.5, T = 4000$.



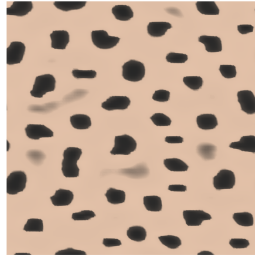
(a)



(b)



(c)



(d)

Figure 10: On random rough surface \mathcal{M} with parameters in Table 1 and Table 2, actual animal coat patterns simulation results: (a) emperor angelfish in [26]; (b) genet in [1]; (c) plecostomus in [12]; (d) cheetah in [46].

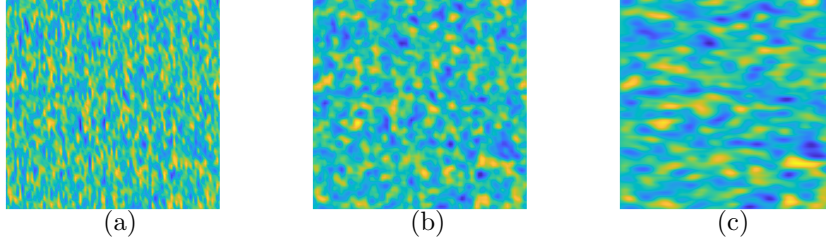


Figure 11: Rough surfaces \mathcal{S} with $\kappa = 2$ and the number of filter steps $J = 15$, under various filter-diffusion tensors \mathcal{F} : (a) $\mathcal{F} = \text{diag}(0.01, 1)$, (b) $\mathcal{F} = \text{diag}(1, 1)$, (c) $\mathcal{F} = \text{diag}(5, 1)$.

type \mathcal{M} . Similar to the scaling in (7), we define \mathcal{S} only by nodal values

$$\left\{ [X, Y, Z] : Z = \frac{\delta_{\mathcal{S}}}{\|\tilde{Z}_J\|_{\infty}} \tilde{Z}_J \right\} \subset \mathcal{S},$$

for some amplitude $\delta_{\mathcal{S}} > 0$.

Figure 11(a, b, c) shows the rough surfaces \mathcal{S} derived for fixed $n_X = 90$, $n_Y = n_X$, $\kappa = 2$ and $J = 15$ filter steps under filter-diffusion tensors

$$\mathcal{F} \in \{\text{diag}(0.01, 1), \text{diag}(1, 1), \text{diag}(5, 1)\},$$

respectively. Taking $\mathcal{F}(1, 1) = 1$ yields a rough surface \mathcal{S} which is similar to a rough surface \mathcal{M} with equal frequencies M, N (cf. Figure 2). Taking $\mathcal{F}(1, 1) = 0.01$ scales down space in the x -direction, yielding a rough surface \mathcal{S} which is similar to a rough surface \mathcal{M} with a larger frequency M , $M > N$. Conversely, taking $\mathcal{F}(1, 1) = 5$, a rough surface \mathcal{S} is obtained which is similar to \mathcal{M} with a smaller frequency M , $M < N$.

To reproduce the properties of surface \mathcal{M} , the required value of filter-diffusion tensors \mathcal{F} and number J of filtering steps will depend on the density of the given data points $[X, Y]$. For fixed amplitude $\delta_{\mathcal{S}} = 1E - 3$ and $n_X = 90$, $n_Y = n_X$, Table 3 gives values of κ , \mathcal{F} and the number of filtering steps J to generate surfaces that give good qualitative agreement with the rough surfaces \mathcal{M} in (7) for various M , N . Figure 2 gives a comparison showing that rough surfaces \mathcal{S} by heat filters (column 2) are qualitatively similar to our earlier surfaces \mathcal{M} by (7) (see column 1).

While not the focus of the current work, our construction methods for \mathcal{S} can be extended to generate rough closed manifolds which can be used as the surfaces for the numerical approximation of PDEs. See Figure 12 for a graphical illustration of rough closed manifolds generated by type- \mathcal{M} and type- \mathcal{S} approaches respectively. Figure 12(a) was obtained by applying the type- \mathcal{M} procedure to the parameter space $(\theta, \phi) \in [0, 2\pi] \times [0, \pi]$ with roughness added to the constant function $r = 1$. Figure 12(b) was obtained by adding noise to $r = 1$ for points on the unit sphere. In contrast to that in (13), the heat filter here makes use of the discrete Laplace-Beltrami operator for the rough sphere.

Table 3: Coefficients for constructing the surfaces \mathcal{S} that appear in the second column of Figure 2. Parameters are chosen to give qualitative agreement with the rough surfaces \mathcal{M} (7) with $\delta_{\mathcal{S}} = 1E-3$, $n_X = 90 = n_Y$

\mathcal{M} in (7)	\mathcal{S} by heat filter		
	κ	\mathcal{F}	filter number
$[M, N] = [5, 5]$	5	diag(1, 1)	15
$[M, N] = [5, 15]$	8	diag(1, 0.01)	10
$[M, N] = [15, 15]$	0.2	diag(20, 20)	2

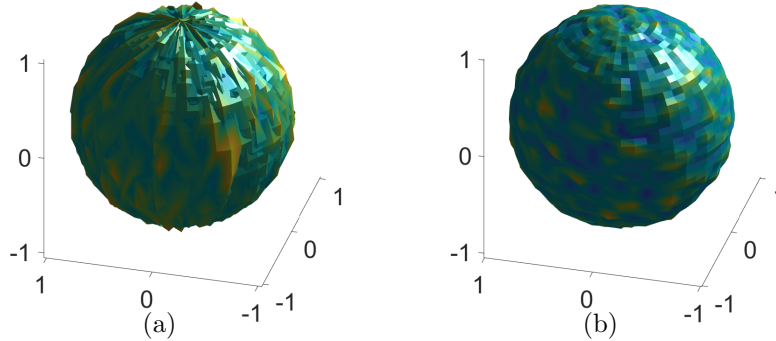


Figure 12: Graphical illustration of rough closed manifolds by (a) type- \mathcal{M} , and (b) type- \mathcal{S} approaches on parameter size and manifold respectively.

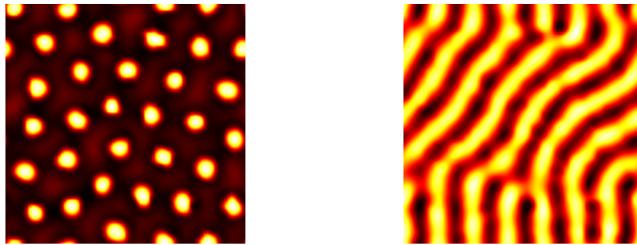


Figure 13: For $\delta_S = 0.1$, $n_X = 90$, $n_Y = n_X$, spot and stripe patterns on a rough surface \mathcal{S} with number of filter steps $J = 15$, $\mathcal{F} = \text{diag}(1, 1)$, and $\kappa = 5$. These values from Table 3 give a rough surface similar to \mathcal{M} with $M = 5, N = 15$. Parameters for spots and stripes are set according to Table 1.

The FDM in Section 3 can be used to solve PDEs on rough surfaces \mathcal{S} . The only difference in the method is that we no longer have the parametric equation to calculate the metric tensor G in (2) and hence the diffusion tensor \mathcal{A} in (13). Instead of computing metric tensor G analytically as in Section 3 and 4, centered finite difference formulas are applied to approximate the metric tensor G . For solving reaction-diffusion systems on rough surfaces \mathcal{S} , we set initial conditions to be steady state solutions on a zero amplitude rough surface \mathcal{M} (7). Figure 13 plots the spot and stripe patterns on a rough surface \mathcal{S} using the reaction-diffusion parameters provided in Table 1. As shown in the second line of Table 3, rough surface \mathcal{S} takes $\kappa = 5$, $\mathcal{F} = \text{diag}(1, 1)$ with $J = 15$ filter steps to approximate rough surface \mathcal{M} with $M = 5, N = 5$. It can be seen that the spot and stripe patterns generated on \mathcal{S} are similar to those on \mathcal{M} under parameters $M = 5, N = 5$, $\delta_{\mathcal{M}} = 0.1$ (see the third row of Figure 5).

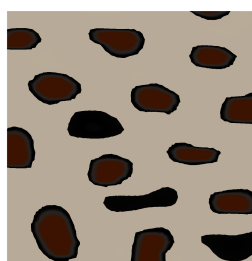
We conclude by simulating the same set of animal coats displayed in Figure 1 using Turing models on rough surfaces \mathcal{S} with parameters set according to Table 1 and Table 4. Figure 14 demonstrates again that adding surface roughness into the process of pattern generation can indeed provide more varied simulations for animal coats. Moreover, the patterns on surface \mathcal{S} provide valid simulations just like \mathcal{M} .

Table 4: Parameters for animal coats simulation on \mathcal{S} with $n_X = n_Y = 90$

		κ	\mathcal{F}	J	τ	T	δ_S
Emperor angelfish [26]	Figure 14 (a)	5	$\text{diag}(1, 1)$	15	0.5	400	0.05
Genet [1]	Figure 14 (b)	8	$\text{diag}(1, 0.01)$	10	0.5	800	0.1
Plecostomus [12]	Figure 14 (c)	8	$\text{diag}(1, 0.01)$	10	0.5	3000	0.1
Cheetah [46]	Figure 14 (d)	0.2	$\text{diag}(20, 20)$	2	0.5	400	0.05



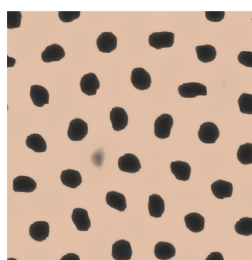
(a)



(b)



(c)



(d)

Figure 14: On random rough surface \mathcal{S} with parameters in Table 1 and Table 4, actual animal coat patterns simulation results: (a) emperor angelfish in [26]; (b) genet in [1]; (c) plecostomus in [12]; (d) cheetah in [46].

6 Conclusion

In this paper, we discussed pattern formation on rough surfaces, with the surface characterized by two different methods: spatial frequency and discretized heat filters. The patterns generated on random rough surfaces of different amplitudes and spatial frequencies are illustrated, and the simulation results indicate that the patterns became relatively more irregular as amplitude increases. The change of spatial frequencies on the x and y axes will also lead to pattern deformation along the x and y directions. Numerical results indicate that combining reaction-diffusion systems with rough surfaces can provide better simulations for animal coat patterns in the real world. What's more, the method for generating rough surfaces by heat filters can be further applied to obtain closed rough manifolds. We plan to explore this generalization in future work.

Appendix: Finite difference algorithm for the heat equation

The heat equation (11) on a rough surface defined over the parameter space $\mathcal{I}^2 = [-1, 1]^2$ is considered. The set of discrete data points on \mathcal{I}^2 are defined as:

$$[X, Y] := \left\{ \left\{ (x_1^i, x_2^j) \right\}_{i=1}^{n_X} \right\}_{j=1}^{n_Y} \in \mathbb{R}^{n_X n_Y \times 2},$$

with mesh size h_{x_1}, h_{x_2} on each axis. To fully discretize (12), we require discretization of the Laplacian-Beltrami operator. For any twice differentiable function $u : \mathcal{I}^2 \rightarrow \mathbb{R}$, we introduce differentiation matrices $\mathcal{D}_k \in \mathbb{R}^{n_X n_Y \times n_X n_Y}$, $k \in \{1, 2\}$ satisfying periodic boundary condition (11b) as follows. Using a second-order centered finite differences, we have for each point (x_1^i, x_2^j) that

$$\begin{aligned} \frac{\partial u}{\partial x_1}(x_1^i, x_2^j) &= \left[-\frac{1}{2h_{x_1}} \quad \frac{1}{2h_{x_1}} \right] \begin{bmatrix} u(x_1^{i-1}, x_2^j) \\ u(x_1^{i+1}, x_2^j) \end{bmatrix}, \\ \frac{\partial u}{\partial x_2}(x_1^i, x_2^j) &= \left[-\frac{1}{2h_{x_2}} \quad \frac{1}{2h_{x_2}} \right] \begin{bmatrix} u(x_1^i, x_2^{j-1}) \\ u(x_1^i, x_2^{j+1}) \end{bmatrix}. \end{aligned}$$

The following fictitious node approach is applied to deal with the periodic boundary conditions:

$$\begin{aligned} u(x_1^0, x_2^j) &= u(x_1^{n_X-1}, x_2^j), \quad u(x_1^{n_X+1}, x_2^j) = u(x_1^2, x_2^j), \quad u(x_1^i, x_2^0) = u(x_1^i, x_2^{n_Y-1}), \\ u(x_1^i, x_2^{n_Y+1}) &= u(x_1^i, x_2^2), \quad u(x_1^1, x_2^j) = u(x_1^{n_X}, x_2^j), \quad u(x_1^i, x_2^1) = u(x_1^i, x_2^{n_Y}). \end{aligned}$$

By assembling all points in $[X, Y]$, the nodal values of $\frac{\partial u}{\partial x_k}$ ($k = 1, 2$) at $[X, Y]$ can be obtained by

$$\frac{\partial u}{\partial x_k}(X, Y) \approx \mathcal{D}_k u(X, Y), \quad \text{for } k \in \{1, 2\},$$

where $u(X, Y) := [u(x_1^1, x_2^1), \dots, u(x_1^{n_x}, x_2^1), \dots, u(x_1^1, x_2^{n_y}), \dots, u(x_1^{n_x}, x_2^{n_y})]^T$ is the vector of nodal function values and differential matrices $\mathcal{D}_k \in \mathbb{R}^{n_x n_y \times n_x n_y}$ are in the form of

$$\mathcal{D}_1 = \begin{bmatrix} D_1^B & \cdots & 0 \\ \vdots & \ddots & \vdots \\ 0 & \cdots & D_1^B \end{bmatrix}, \quad D_1^B = \frac{1}{2h_{x_1}} \begin{bmatrix} 0 & 1 & 0 & \cdots & 0 & -1 & 0 \\ -1 & 0 & 1 & \cdots & 0 & 0 & 0 \\ \vdots & \vdots & \vdots & \ddots & \vdots & \vdots & \vdots \\ 0 & 0 & 0 & \cdots & -1 & 0 & 1 \\ 1 & 0 & 0 & \cdots & 0 & 0 & -1 \end{bmatrix},$$

and

$$\mathcal{D}_2 = \begin{bmatrix} 0 & D_2^B & 0 & \cdots & 0 & -D_2^B & 0 \\ -D_2^B & 0 & D_2^B & \cdots & 0 & 0 & 0 \\ \vdots & \vdots & \vdots & \ddots & \vdots & \vdots & \vdots \\ 0 & 0 & 0 & \cdots & -D_2^B & 0 & D_2^B \\ D_2^B & 0 & 0 & \cdots & 0 & 0 & -D_2^B \end{bmatrix}, \quad D_2^B = \frac{1}{2h_{x_2}} \begin{bmatrix} 1 & \cdots & 0 \\ \vdots & \ddots & \vdots \\ 0 & \cdots & 1 \end{bmatrix},$$

with $D_k^B \in \mathbb{R}^{n_x \times n_x}$, $k \in \{1, 2\}$.

References

- [1] <https://commons.wikimedia.org/wiki/Category:Genetta%20tigrina?uselang=it>.
- [2] R. ASAI, E. TAGUCHI, Y. KUME, M. SAITO, AND S. KONDO, *Zebrafish Leopard gene as a component of the putative reaction-diffusion system*, Mechanisms of Development, (1999), p. 6.
- [3] U. M. ASCHER AND L. R. PETZOLD, *Computer methods for ordinary differential equations and differential-algebraic equations*, Society for Industrial and Applied Mathematics, 1998.
- [4] D. AVITABILE, V. F. BREÑ MEDINA, AND M. J. WARD, *Spot dynamics in a reaction-diffusion model of plant root hair initiation*, SIAM Journal on Applied Mathematics, 78 (2018), pp. 291–319.
- [5] M. BERTALMIÓ, L. CHENG, S. OSHER, AND G. SAPIRO, *Variational problems and partial differential equations on implicit surfaces*, Journal of Computational Physics, 174 (2001), pp. 759–780.
- [6] H. A. BROOKS AND P. C. BRESSLOFF, *A mechanism for turing pattern formation with active and passive transport*, SIAM Journal on Applied Dynamical Systems, 15 (2016), pp. 1823–1843.
- [7] P. CARTER AND A. DOELMAN, *Traveling stripes in the klausmeier model of vegetation pattern formation*, SIAM Journal on Applied Mathematics, 78 (2018), pp. 3213–3237.

- [8] M. CHEN AND L. LING, *Kernel-based meshless collocation methods for solving coupled bulk-surface partial differential equations*, Journal of Scientific Computing, 81 (2019), pp. 375–391.
- [9] ———, *Extrinsic meshless collocation methods for PDEs on manifolds*, SIAM J. Num. Anal., 58 (2020), pp. 988–1007.
- [10] K. C. CHEUNG AND L. LING, *A kernel-based embedding method and convergence analysis for surfaces PDEs*, SIAM J. Sci. Comput., 40 (2018), pp. A266–A287.
- [11] A. CHU, *Closest point methods with polyharmonic spline radial basis functions and local refinement*, PhD thesis, University of British Columbia, 2021.
- [12] CONTRIBUTORS TO WIKIMEDIA PROJECTS. <https://en.wikipedia.org/wiki/Plecostomus>.
- [13] J. DONG, *Avoiding collisions and pattern formation in flocks*, SIAM Journal on Applied Mathematics, 81 (2021), pp. 2111–2129.
- [14] Q. DU, M. D. GUNZBURGER, AND L. JU, *Voronoi-based finite volume methods, optimal Voronoi meshes, and PDEs on the sphere*, Computer Methods in Applied Mechanics and Engineering, 192 (2003), pp. 3933–3957.
- [15] Q. DU AND L. JU, *Finite volume methods on spheres and spherical centroidal voronoi meshes*, SIAM Journal on Numerical Analysis, 43 (2005), pp. 1673–1692.
- [16] G. DZIUK AND C. M. ELLIOTT, *Finite element methods for surface PDEs*, Acta Numerica, 22 (2013), pp. 289–396.
- [17] ———, *The Science of Fractal Images*, vol. 22, Cambridge University Press, 2013.
- [18] P. C. FIFE, *Mathematical aspects of reacting and diffusing systems*, 28 (1979).
- [19] E. J. FUSELIER AND G. B. WRIGHT, *A high-order kernel method for diffusion and reaction-diffusion equations on surfaces*, Journal of scientific computing, 56 (2013), pp. 535–565.
- [20] E. GADELMAWLA, M. KOURA, T. MAKSOUD, I. ELEWA, AND H. SOLIMAN, *Roughness parameters*, Journal of Materials Processing Technology, 123 (2002), pp. 133–145.
- [21] A. GIERER AND H. MEINHARDT, *A theory of biological pattern formation*, vol. 12, 1972.

- [22] G. HU, Z. QIAO, AND T. TANG, *Moving finite element simulations for reaction-diffusion systems*, Advances in Applied Mathematics and Mechanics, (2015).
- [23] Y. Z. HU AND K. TONDER, *Simulation of 3-D random rough surface by 2-D digital filter and fourier analysis*, International journal of machine tools and manufacture, 32 (1992), pp. 83–90.
- [24] W. HUANG AND M. MULTERER, *Isogeometric analysis of diffusion problems on random surfaces*, arXiv preprint arXiv:2109.03761, (2021).
- [25] V. KLIKA, M. KOZÁK, AND E. A. GAFFNEY, *Domain size driven instability: Self-organization in systems with advection*, SIAM Journal on Applied Mathematics, 78 (2018), pp. 2298–2322.
- [26] A. KOK. https://commons.wikimedia.org/wiki/File:Pomocanthus_imperator_facing_right.jpg, 2014.
- [27] S. KONDO AND R. ASAI, *A reaction-diffusion wave on the skin of the marine angelfish pomacanthus*, Nature, 376 (1995), pp. 765–768.
- [28] O. LAKKIS, A. MADZVAMUSE, AND C. VENKATARAMAN, *Implicit-explicit timestepping with finite element approximation of reaction-diffusion systems on evolving domains*, SIAM Journal on Numerical Analysis, 51 (2013), p. 2013.
- [29] E. LEHTO, V. SHANKAR, AND G. B. WRIGHT, *A radial basis function (RBF) compact finite difference (FD) scheme for reaction-diffusion equations on surfaces*, SIAM Journal on Scientific Computing, 39 (2017), pp. A2129–A2151.
- [30] S. LI AND L. LING, *Complex pattern formations by spatial varying parameters*, Advances in Applied Mathematics and Mechanics, 12 (2020), pp. 1327–1352.
- [31] S. LI AND Z. QIAO, *A meshless collocation method with a global refinement strategy for reaction-diffusion systems on evolving domains*, Discrete & Continuous Dynamical Systems–B, (2021).
- [32] J. LU, F. BAGINSKI, AND X. REN, *Equilibrium configurations of boundary droplets in a self-organizing inhibitory system*, SIAM Journal on Applied Dynamical Systems, 17 (2018), pp. 1353–1376.
- [33] D. B. McDONALD, W. J. GRANTHAM, W. L. TABOR, AND M. J. MURPHY, *Global and local optimization using radial basis function response surface models*, Applied Mathematical Modelling, 31 (2007), pp. 2095–2110.
- [34] J. MURRAY, *A pattern formation mechanism and its application to mammalian coat markings*, 1980.

- [35] J. MURRAY, *A pre-pattern formation mechanism for animal coat markings*, Journal of Theoretical Biology, 88 (1981), pp. 161 – 199.
- [36] M. A. OLSHANSKII, A. REUSKEN, AND J. GRANDE, *A finite element method for elliptic equations on surfaces*, SIAM Journal on Numerical Analysis, 47 (2009), pp. 3339–3358.
- [37] P. PAWLUS, R. REIZER, AND M. WIECZOROWSKI, *A review of methods of random surface topography modeling*, Tribology International, (2020), p. 106530.
- [38] Z. QIAO, *Numerical investigations of the dynamical behaviors and instabilities for the gierer-meinhardt system*, Communications in Computational Physics, 3 (2008), pp. 406–426.
- [39] S. J. RUUTH, *Implicit-explicit methods for reaction-diffusion problems in pattern formation*, Journal of Mathematical Biology, 34 (1994).
- [40] S. J. RUUTH AND B. MERRIMAN, *A simple embedding method for solving partial differential equations on surfaces*, Journal of Computational Physics, 227 (2008), pp. 1943–1961.
- [41] V. SHANKAR, G. B. WRIGHT, AND A. NARAYAN, *A robust hyperviscosity formulation for stable RBF-FD discretizations of advection-diffusion-reaction equations on manifolds*, SIAM Journal on Scientific Computing, 42 (2020), pp. A2371–A2401.
- [42] R. SHI, B. WANG, Z. YAN, Z. WANG, AND L. DONG, *Effect of surface topography parameters on friction and wear of random rough surface*, Materials, 12 (2019), p. 2762.
- [43] B. SJODIN, *How to generate random surfaces in COMSOL multiphysics®*.
- [44] P. SUCHDE AND J. KUHNERT, *A meshfree generalized finite difference method for surface PDEs*, Computers & Mathematics with Applications, 78 (2019), pp. 2789–2805.
- [45] Z. TANG, Z. FU, M. CHEN, AND L. LING, *A localized extrinsic collocation method for Turing pattern formations on surfaces*, Applied Mathematics Letters, 122 (2021), p. 107534.
- [46] TASNIM. <https://www.tasnimnews.com/fa/news/1394/09/15/935574/>.
- [47] A. M. TURING, *The chemical basis of morphogenesis*, Phil. Trans. R. Soc. Lond., 237 (1952), pp. 37–72.